

Supplementary Material

Fate of Transient Isomer of CH₂I₂: Mechanism and Origin of Ionic Photoproducts Formation Unveiled by Time-Resolved X-ray Liquidography

Sungjun Park^{†,a,b}, Jungkweon Choi^{†,b}, Hosung Ki^b, Kyung Hwan Kim^c, Key Young Oang^d,
Heegwang Roh^a, Joonghan Kim^e, Shunsuke Nozawa^f, Tokushi Sato^{§,f}, Shin-ichi Adachi^{f,g},
Jeongho Kim^{*h} and Hyotcherl Ihee^{*a,b}

^aDepartment of Chemistry and KI for the BioCentury, Korea Advanced Institute of Science and Technology (KAIST), Daejeon 34141, Republic of Korea

^bCenter for Nanomaterials and Chemical Reactions, Institute for Basic Science (IBS), Daejeon 34141, Republic of Korea

^cDepartment of Chemistry, Pohang University of Science and Technology (POSTECH), Pohang 37673, South Korea

^dRadiation Center for Ultrafast Science, Quantum Optics Division, Korea Atomic Energy Research Institute (KAERI), Daejeon 34057, Republic of Korea

^eDepartment of Chemistry, The Catholic University of Korea, Bucheon 14662, Republic of Korea

^fInstitute of Materials Structure Science, High Energy Accelerator Research Organization, 1-1 Oho, Tsukuba, Ibaraki 305-0801, Japan

^gDepartment of Materials Structure Science, School of High Energy Accelerator Science, the Graduate University for Advanced Studies, 1-1 Oho, Tsukuba, Ibaraki 305-0801, Japan

^hDepartment of Chemistry, Inha University, 100 Inha-ro, Michuhol-gu, Incheon, 22212, Republic of Korea

[§]Present address: Center for Free-Electron Laser Science, Deutsches Elektronen Synchrotron, Notkestrasse 85, 22607 Hamburg, Germany; European XFEL GmbH, Holzkoppel 4, 22869 Schenefeld, Germany

[†]These authors equally contributed to this work

*** Corresponding Author**

E-mail: jkim5@inha.ac.kr, hyotcherl.ihee@kaist.ac.kr

Table of Contents

<u>SI Texts</u>	Pages
1. Methods and Data Acquisition	S3
2. Data Processing	S4
3. Global Fit Analysis	S5 – S7
4. Molecular Dynamics Simulation for Solute-Solvent Cross Term	S8
5. Computational Details	S9
6. Sine-Fourier Transform	S10
7. Reference	S16 – S17

<u>SI Figures</u>	Pages
1. Figure S1	S11
2. Figure S2	S12
3. Figure S3	S13
4. Figure S4	S14
5. Figure S5	S15

1. Methods and Data Acquisition

The TRXL experiment was conducted with the laser pump–X-ray probe scheme at the beamline NW14 at KEK. The detailed setup of TRXL experiment is described in the literature.^{1–4} The 50 mM CH₂I₂ (Sigma-Aldrich, 99.9 %) solution was prepared in methanol. The sample solution was circulated through a high-pressure sapphire slit nozzle. A stable 300- μ m-thick liquid sheet was produced by a sapphire nozzle with the sample solution circulated at a speed (\sim 3 m/s), ensuring to provide a fresh sample for each pair of laser and X-ray pulses. Third harmonic generation of the output pulses from an amplified Ti:Sapphire laser system provided femtosecond pulses at 267 nm center wavelength at a repetition rate of 1 kHz. To avoid the multiphoton excitation of the sample, the frequency-tripled laser pulses were stretched to \sim 2 ps by passage through fused silica rods. The laser beam was focused by a lens to a spot with a diameter of 300 μ m, where the laser beam overlaps with the X-ray beam with the crossing angle of 10°. At the sample, the pulse energy was 240 μ J, yielding a fluence of \sim 2.6 mJ/mm². The laser pulses were synchronized with X-ray pulses from the synchrotron by an active feedback control loop that adjusts the laser oscillator cavity length, and the relative time delay between the laser and X-ray pulses were controlled electronically. The time-delayed X-ray pulses were selected by using a synchronized mechanical chopper. A multilayer optic coated with depth-graded Ru/C layers ($d = 40$ Å, NTT Advanced Technology, Japan) produced a Gaussian-type X-ray spectrum with an energy bandwidth of \sim 5 % at the center wavelength of 0.71 Å from the undulator spectrum. The 150-ps X-ray pulse with 3×10^8 photons per pulse was focused into a 260×290 μ m² spot at the sample. The scattering patterns were collected by an area detector (MarCCD165, Mar USA) with a sample-to-detector distance of 40 mm. To probe the photodissociation of CH₂I₂, the scattering signals were collected at various pump-probe time delays ($\Delta t = 150$ ps, 300ps, 1 ns, 3 ns, 10 ns, 30 ns, 50 ns, 100 ns, 300 ns, 1 μ s, and 3 μ s). The scattering signal at a negative time delay, $S(q, -3$ ns), which contains the signal from an unexcited sample, was subtracted from the signals at other positive time delays to obtain the difference scattering signals, $\Delta S(q, t)$.

2. Data Processing

The two-dimensional scattering images were transformed into one-dimensional scattering curves via azimuthal integration as a function of the momentum transfer $q = (4\pi/\lambda)\sin\theta$, where λ is the wavelength of X-ray and 2θ is the scattering angle. The intensity of scattering curves were normalized by the area under curve at q from 4.0 to 8.0 \AA^{-1} . After normalization, the difference scattering curves were obtained by subtracting the scattering curve at a negative time delay ($t = -3$ ns) from the scattering curves at positive time delays. The difference scattering curves were further scaled to the unperturbed scattering intensity from one methanol molecule so that the scattering intensity can be put on an absolute intensity scale corresponding to one solvent molecule. The difference radial intensity, $r^2\Delta R(r,t)$, represents the radial electron density change as a function of interatomic distance r in real space, and was obtained by sine-Fourier transform of the $q\Delta S(q,t)$ curves according to the following relation:

$$r^2\Delta R(r, t) = \frac{r}{2\pi^2} \int_0^\infty q\Delta S(q)\sin(q, t)e^{-q^2\alpha} dq$$

The Gaussian damping constant $\alpha = 0.03 \text{ \AA}^2$ was employed to account for the finite experimental q range.

3. Global Fit Analysis

Theoretical X-ray scattering intensities were calculated using the standard diffuse X-ray scattering formula. The difference X-ray scattering curve, $\Delta S(q,t)_{theory}$, includes three components, (i) solute-only term, (ii) solute-solvent cross term (so-called cage term), and (iii) solvent-only term as follows:

$$\begin{aligned}\Delta S(q, t) &= \Delta S_{solute}(q, t) + \Delta S_{solute-solvent}(q, t) + \Delta S_{solvent}(q, t) \\ &= \Delta S_{solute-related}(q, t) + \Delta S_{solvent}(q, t) \\ &= \frac{1}{R} \left[\sum_k c_k(t) S_k(q) - S_g(q) \sum_k c_k(0) \right] \\ &\quad + \left[\left(\frac{\partial S}{\partial T} \right)_\rho \Delta T(t) + \left(\frac{\partial S}{\partial \rho} \right)_T \Delta \rho(t) \right]\end{aligned}$$

where R is the number ratio of the solvent molecules to solute molecules, k is the index of the solute species (reactants, intermediates and products), $c_k(t)$ is the fractional concentration of k th species at time delay t , $S_k(q)$ is the solute-related (that is, solute-only and cage terms) scattering curve of k th species, and $S_g(q)$ is the scattering curve of the ground state reactant. The temperature and density changes, $\Delta T(t)$ and $\Delta \rho(t)$, were obtained by solving the hydrodynamics equations, in which the heat released during the entire course of reaction was estimated based on the excitation energy, quantum yield, and relative energies of intermediates and products with respect to the ground-state reactant.

The solute-only term was calculated using the well-known Debye equation:

$$I(q) = \sum_i f_i(q)^2 + \sum_i \sum_j f_i(q) f_j(q) \sin(qr_{ij}) / qr_{ij}$$

where $f_i(q)$ and $f_j(q)$ are the atomic form factors for atom types i and j . The solute-only term, $\Delta S(q,t)_{solute}$, was further calculated using the structural parameters or modified ones from the DFT structures. As fitting parameters, we used the C-I bond lengths (of CH_2I_2 , CH_2I^+ , CH_2I^- , and *iso*- $\text{CH}_2\text{I-I}$), I-I bond lengths (of I_2^- , I_3^- , and *iso*- $\text{CH}_2\text{I-I}$), and the C-I-I bond angle of *iso*- $\text{CH}_2\text{I-I}$ to refine the geometry of the chemical species involved in the photodissociation of CH_2I_2 . The solute-solvent cross term, $\Delta S(q,t)_{solute-solvent}$, was calculated from the pair distribution functions obtained from MD simulations. We took into account the extra charge

for ionic species. For example, for CH_2I^+ , the atomic form factor for the Te atom, which has one less electron than the I atom, was used to account for the one positive charge. For this reason, $\text{CH}_2\text{I}^\cdot$ and CH_2I^+ give slightly different (practically negligible, though) solute-only terms even when all structural parameters are the same as shown in Figure S2a. The solvent-only term, $\Delta S(q,t)_{\text{solvent}}$, was obtained from a separate solvent-heating experiment. The solvent-only term consists of two terms involving differentials, $(\partial S/\partial T)_\rho$ and $(\partial S/\partial \rho)_T$. $(\partial S/\partial T)_\rho$ is the change in the scattering intensity with respect to a temperature change at constant density and $(\partial S/\partial \rho)_T$ is the change in the scattering intensity with respect to a density change in the solvent at constant temperature.⁵⁻⁷ $\Delta T(t)$ and $\Delta \rho(t)$ are the time-dependent changes in the temperature and density of the solvent, respectively, and were obtained with the hydrodynamic equation.(ref) To obtain $\Delta T(t)$ and $\Delta \rho(t)$, we first estimated the heat $Q(t)$ in the unit of J/mol released to the solvent as a function of time by using the following equation (S1):

$$\begin{aligned}
 Q(t) &= \text{Energy}(t=0) - \text{Energy}(t) \\
 &= \frac{N_A}{R} f_{\text{exc}} \left[\sum_k (E_g + hv) c_k(0) - \sum_k E_k c_k(t) \right] \\
 &\quad + \frac{N_A}{R} f_{\text{exc}} f_{\text{fast}} [1 - \exp(-t/k_{\text{fast}})]
 \end{aligned}$$

where N_A is Avogadro's number, R is the ratio of the number of solvent molecules to that of solute molecules, $c_k(t)$ is the unitless fractional concentration of species k at time t , E_g is the absolute energy of the ground state molecule in the unit of J/molecule, hv is the excitation energy, E_k is the energy of species k , f_{exc} is the excitation ratio, f_{fast} is the ratio of a fast-decaying component, and k_{fast} is the rate constant for vibrational cooling. The absolute energy of each species was determined by DFT/TDDFT calculations. Here, the cooling rate, k_{fast} , is assumed to be $(10 \text{ ps})^{-1}$ because the vibrational cooling process occurs much faster than our temporal resolution of 100 ps. Then, based on the obtained $Q(t)$, we calculated the pressure change $\Delta P(t)$, temperature change $\Delta T(t)$, and density change $\Delta \rho(t)$ by solving the following hydrodynamics equation (S2):

$$\Delta P(t) = \frac{\alpha_P}{\chi_T C_V} \int_{-\infty}^t \frac{\partial Q}{\partial t}(\tau) \exp[-\left\{\left(\frac{v_s}{a}\right)(t-\tau)\right\}^2] d\tau$$

$$\Delta T(t) = \frac{Q(t) - (C_V - C_P) \frac{\chi_T}{\alpha_P} \Delta P(t)}{C_P}$$

$$\Delta \rho(t) = \rho_0 [\chi_T \Delta P(t) - \alpha_P \Delta T(t)]$$

where α_P in the unit of K^{-1} is the isobaric thermal expansion coefficient, χ_T in the unit of Pa^{-1} is the isothermal compression coefficient, v_S in the unit of m/s is the speed of sound in the solvent, a in the unit of m is the root-mean-square size of laser spot, C_V in the unit of $\text{J mol}^{-1}\text{K}^{-1}$ is the heat capacity at constant volume, and C_P is the heat capacity at constant pressure.(ref) The estimated temperature and density changes are shown in Figure S5. Time-resolved X-ray solution scattering curves were analyzed by global fit (GF) analysis method using a home-made algorithm. To extract the structural dynamics of CH_2I_2 and all photoproducts from the difference scattering intensities, the maximum likelihood estimation (MLE) method with the χ^2 estimator was employed for each variable parameter.^{8,9} The experimental difference scattering curves, $\Delta S(q,t)$, were fit by the theoretical difference scattering curves using weighted least-squares minimization, whereby the square of the difference between the experimental and the theoretical intensities divided by the standard deviation of the experimental error, i.e., the reduced chi-square (χ^2), was minimized. Since the experimental $\Delta S(q,t)$ curves at various time delays are related to each other through reaction kinetics, they were globally fit by minimizing the sum of “reduced” χ^2 values at all positive time delays.

$$\chi^2 = \frac{1}{N-p-1} \sum_{j=\text{time delay}} \sum_i \frac{(\Delta S_{\text{theory}}(q_i, t_j) - \Delta S_{\text{experiment}}(q_i, t_j))^2}{\sigma_{i,j}^2}$$

where N is the total number of data points along q axis, m is the number of fitting parameters, and $\sigma_{i,j}$ is the standard deviation of the experimental noise present in $\Delta S_{\text{experiment}}(q,t)$ at q_i and time delay t_j . Thereby, sixteen fitting parameters in total including reaction rate constants, the branching ratio of photoproducts, the excitation ratio of photoexcited molecules and the structural parameters of solute molecules were globally determined. The χ^2 minimization was performed using the global optimization package written at LabVIEW and the error analysis was done by a home-made algorithm based on MLE fitting. Since the difference between the experimental and theoretical difference scattering curves is divided by the standard deviation of the experimental error, the reduced χ^2 can in principle have a minimum value of 1, which stands for the theoretically-allowed best fit. The reduced χ^2 is commonly used as a measure of

the goodness of a fit.^{8,9}

4. Molecular Dynamics Simulation for Solute-Solvent Cross Term

The solute-solvent cross term that describes the interaction between the solutes and the solvent was obtained by molecular dynamics (MD) simulation using the program MOLLY.^{10,11} The H1 methanol model was used to describe the force field for methanol molecules.¹² For the MD simulation of the scattering from the solute in its solvation cage, we used one solute molecule such as CH₂I₂, CH₂I⁺, CH₂I[•], *iso*-CH₂I-I, I[•], I⁻, I₂⁻, and I₃⁻ surrounded by 512 methanol molecules in a cubic box whose edge is larger than 25 Å. All the MD simulations were performed with periodic boundary conditions. The structures of solute molecules and the charges on each atom were obtained from DFT calculations and kept constant during the simulation. All simulations were performed at ambient temperature (300 K) with a density of 0.790 g/cm³. The system was equilibrated at 300 K over 200 ps at constant temperature via coupling to a Nose–Hoover thermostat. The time step was 0.5 fs. The simulations were performed in the NVT ensemble, and the trajectories were followed up to 1 ns. The scattering intensity for each molecular configuration was calculated from the radial distribution function, $g_{ij}(r)$, by using our own programs and tabulated atomic form factors.

$$S(q) = \sum_{ij} f_i(q)f_j(q) \left[N_i\delta_{ij} + \frac{N_iN_j}{V} \int_0^\infty \{g_{ij}(r) - 1\} \frac{\sin(qr)}{qr} 4\pi r^2 dr \right]$$

where $f_i(q)$ is the atomic form factor of the i -type atom, N_i is the number of i -type atoms, δ_{ij} is the Kronecker delta, and V is the volume of the box.

5. Computational Details

All chemical species involved in the photodissociation of CH_2I_2 were optimized by density functional theory (DFT) calculations. We used the ωB97X^{13} functional as the DFT exchange-correlation functional because the ωB97X functional can accurately predict the C–I distance in halomethanes and haloethanes.¹⁴ However, in a recent study, the MN12-SX showed better performance for optimizing the molecular structures of photoproducts generated from the photodissociation of CHI_3 .⁹ Thus, we also used the MN12-SX functional in this work. For carbon and hydrogen atoms, aug-cc-pVTZ all-electron basis sets were used and, to consider relativistic effects that arise from the iodine atom, an aug-cc-pVTZ-PP small-core relativistic effective core potential (RECP) was applied.¹⁵ Hereafter, this combination is denoted as AVTZ. For the geometry optimizations of *iso*- $\text{CH}_2\text{I}-\text{I}$, we used the broken-symmetry method to include the biradical character of the isomer. Solvent effects were implicitly included by applying an integral equation formalism polarizable continuum model (IEFPCM) for all the calculations. We also used the coupled-cluster singles and doubles with perturbative triples (CCSD(T)) calculations to obtain more accurate energetics for clarifying critical issues. The geometry optimizations of CH_2I_2 , $\text{CH}_2\text{I}\cdot$, and CH_2I^+ were performed using the CCSD(T)/AVTZ. The subsequent vibrational frequency calculations were also performed to identify the minimum energy structures at the same level. The further single-point calculations were performed using the CCSD(T)/AVQZ (the aug-cc-pVQZ-PP for I and aug-cc-pVQZ for C and H) on the optimized structures by the CCSD(T)/AVTZ. The zero-point energies of the CCSD(T)/AVTZ were used for the further single-point calculations. All calculations were performed using the Gaussian16 programs.¹⁶

6. Sine-Fourier Transform

The difference RDF, $r^2\Delta S(r)$, where r is the interatomic distance, is a measure of the radial electron density change around an excited atom as a function of r in real space. The difference RDF was obtained by sine-Fourier transform of $q\Delta S(q)$ using the following equation:

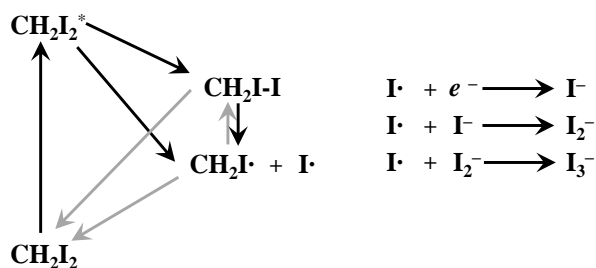
$$r^2\Delta S(r) = \frac{r}{2\pi^2} \int_0^\infty q\Delta S(q) \sin(qr) dq$$

To take account of the finite q range of the experimental data, $r^2\Delta S(r)$ is convoluted with a Gaussian function, $\exp(-q^2\alpha)$, giving the modified $r^2\Delta S(r)$ as follows:

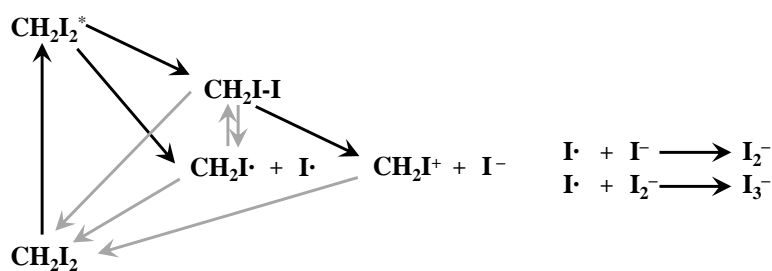
$$r^2\Delta S(r) = \frac{r}{2\pi^2} \int_0^\infty q\Delta S(q) \sin(qr) e^{-q^2\alpha} dq$$

For the damping constant, α , we used a value of 0.03 \AA^2 .

a) Homolysis



b) Heterolysis



c) Solvolysis

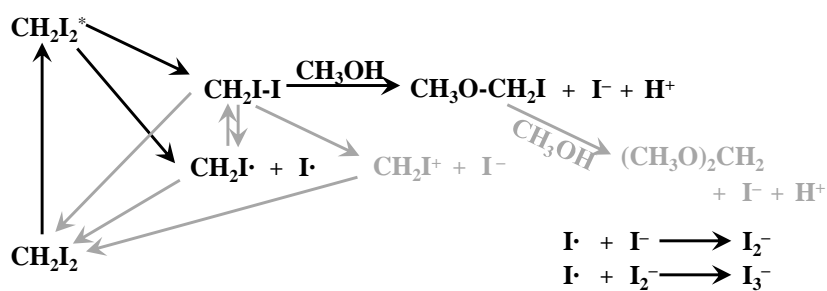


Figure S1. Kinetic models examined in this work. The kinetic frameworks for (a) homolysis with the electron transfer from solvent, (b) heterolysis, and (c) solvolysis are shown. The paths which were considered but whose rates converges to zero are indicated with gray arrows.

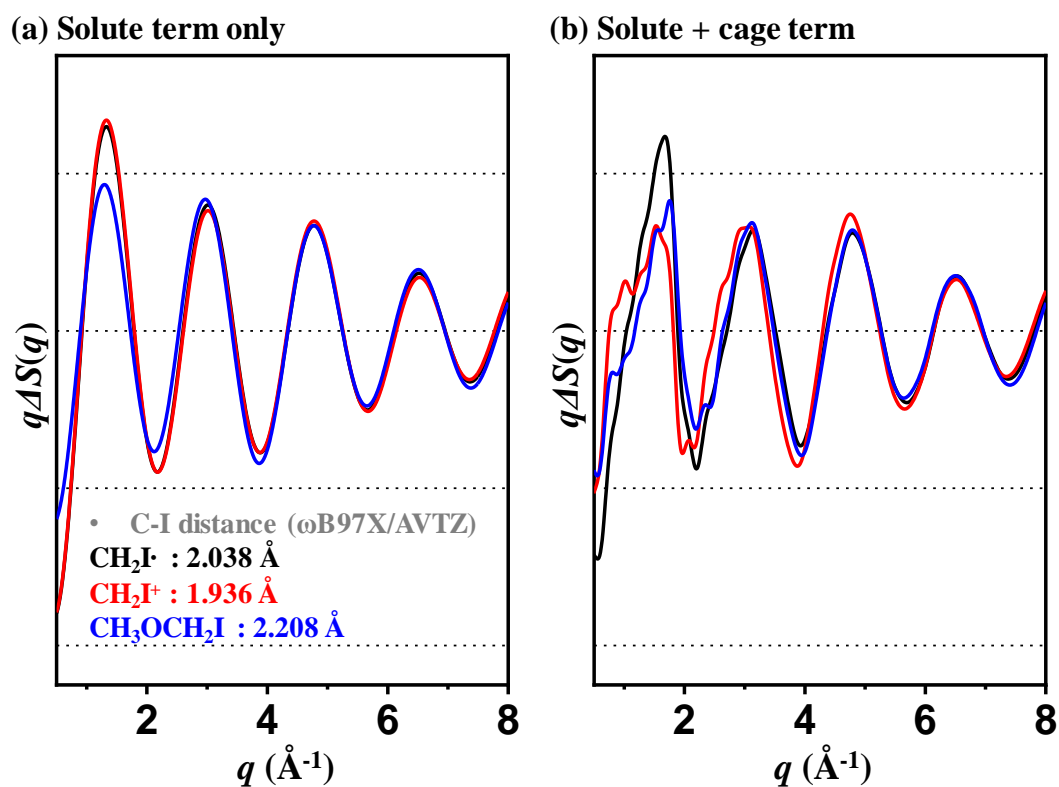


Figure S2. Comparison of the difference scattering signals for the key intermediates **CH₂I•** (black), **CH₂I⁺** (red) and **CH₃OCH₂I** (blue) representing each of the homolysis, heterolysis and solvolysis models. (a) Solute-only term. (b) The sum of solute-only and cage terms. The same C-I distance (2.038 \AA) for all three intermediates was used.

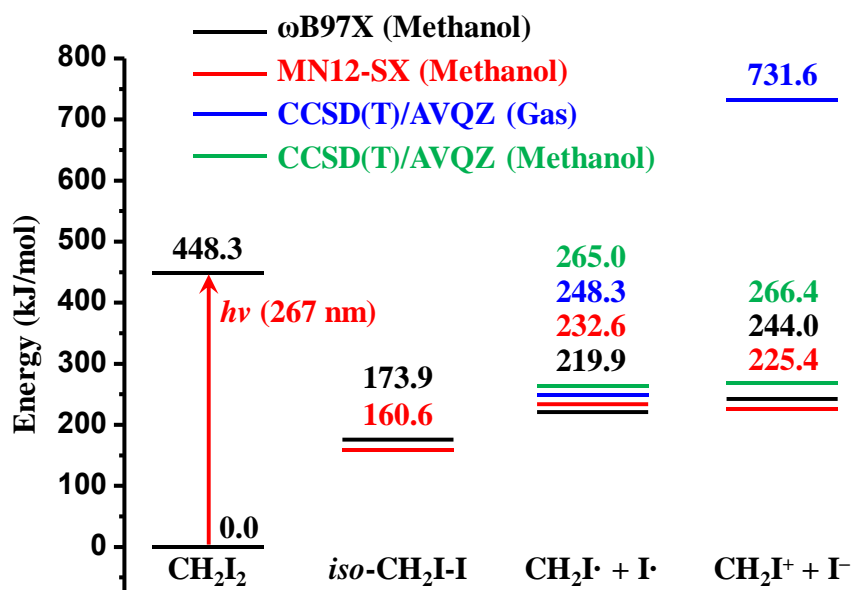


Figure S3. Energies of the chemical species involved in the photodissociation of CH_2I_2 . The energy values calculated by ω B97X/AVTZ, MN12-SX/AVTZ, CCSD(T)/AVQZ (gas), and CCSD(T)/AVQZ (methanol) are indicated in black, red, blue, and green, respectively. The energies shown in the diagram were calculated relative to the energy of the CH_2I_2 parent molecule in the ground state.

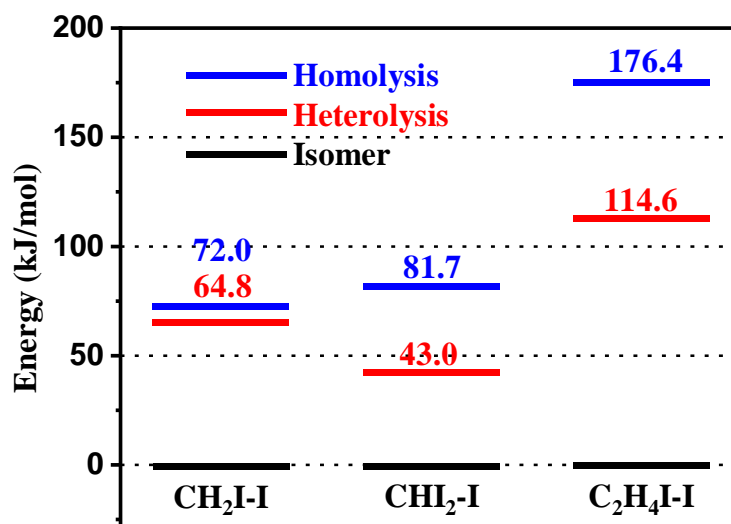


Figure S4. Reaction energies of heterolysis and homolysis for the CH₂I-I, CHI₂-I, and C₂H₄I-I isomers. The reaction energies of homolysis (blue) and heterolysis (red) were calculated by MN12-SX/AVTZ in the methanol environment.

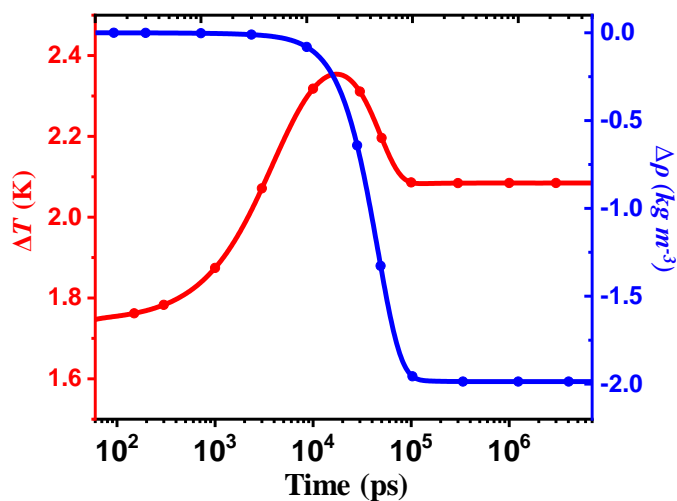


Figure S5. Time-dependent changes of solvent temperature (red) and density (black) induced by photodissociation of CH_2I_2 . Before 10 ns, the heat dissipated from the photoreaction induces the temperature increase at a constant volume. After 10 ns, the thermal expansion occurs and the density of the solvent decreases with ~ 30 ns time constant. The solid lines were obtained from optimized global fits based on the final optimized kinetic model based on heterolysis of *iso*- $\text{CH}_2\text{I-I}$, and dots with error bars were obtained from the fitting of the experimental difference scattering curve at each time delay individually by a linear combination of necessary contributions such as solute, cage, and solvent terms.

7. References

- ¹ M. Chollet, T. Sato, T. Mori, E. Collet, S. Nozawa, R. Tazaki, H. Sawa, S. Adachi, H. Sasaki, A. Tomita, L. Guérin, H. Kawata, M. Daimon, S. Yamamoto, K. Tsuchiya, S. Koshihara, H. Cailleau, J. Takahashi, T. Shioya, and K. Ichiyanagi, *J. Synchrotron Radiat.* **14**, 313 (2007).
- ² K. Ichiyanagi, T. Sato, S. Nozawa, K.H. Kim, J.H. Lee, J. Choi, A. Tomita, H. Ichikawa, S. Adachi, H. Ihee, and S. Koshihara, *J. Synchrotron Radiat.* **16**, 391 (2009).
- ³ K.H. Kim, J.H. Lee, J. Kim, S. Nozawa, T. Sato, A. Tomita, K. Ichiyanagi, H. Ki, J. Kim, S.I. Adachi, and H. Ihee, *Phys. Rev. Lett.* **110**, 1 (2013).
- ⁴ K.H. Kim, J. Kim, J.H. Lee, and H. Ihee, *Struct. Dyn.* **1**, (2014).
- ⁵ T.K. Kim, M. Lorenc, J.H. Lee, M. Lo Russo, J. Kim, M. Cammarata, Q. Kong, S. Noel, A. Plech, M. Wulff, and H. Ihee, *Proc. Natl. Acad. Sci. U. S. A.* **103**, 9410 (2006).
- ⁶ M. Cammarata, M. Lorenc, T.K. Kim, J.H. Lee, Q.Y. Kong, E. Pontecorvo, M. Lo Russo, G. Schiró, A. Cupane, M. Wulff, and H. Ihee, *J. Chem. Phys.* **124**, 1 (2006).
- ⁷ H. Ihee, M. Lorenc, T.K. Kim, Q.Y. Kong, M. Cammarata, J.H. Lee, S. Bratos, and M. Wulff, *Science (80-.)*. **309**, 1223 (2005).
- ⁸ S. Jun, J.H. Lee, J. Kim, J. Kim, K.H. Kim, Q. Kong, T.K. Kim, M. Lo Russo, M. Wulff, and H. Ihee, *Phys. Chem. Chem. Phys.* **12**, 11536 (2010).
- ⁹ C.W. Ahn, H. Ki, J. Kim, J. Kim, S. Park, Y. Lee, K.H. Kim, Q. Kong, J. Moon, M.N. Pedersen, M. Wulff, and H. Ihee, *J. Phys. Chem. Lett.* **9**, 647 (2018).
- ¹⁰ K. Refson, *Comput. Phys. Commun.* **126**, 310 (2000).
- ¹¹ Q. Kong, J.H. Lee, K.H. Kim, J. Kim, M. Wulff, H. Ihee, and M.H.J. Koch, *J. Am. Chem. Soc.* **132**, 2600 (2010).
- ¹² A. Idrissi, R.D. Oparin, S.P. Krishtal, S. V. Krupin, E.A. Vorobiev, A.I. Frolov, L. Dubois, and M.G. Kiselev, *Faraday Discuss.* **167**, 551 (2013).
- ¹³ J. Da Chai and M. Head-Gordon, *J. Chem. Phys.* **128**, 0 (2008).
- ¹⁴ J. Kim, T.K. Kim, and H. Ihee, *J. Phys. Chem. A* **115**, 1264 (2011).
- ¹⁵ F. Weigend and A. Baldes, *J. Chem. Phys.* **133**, (2010).
- ¹⁶ Frisch, M. J.; Trucks, G. W.; Schlegel, H. B.; Scuseria, G. E.; Robb, M. A.; Cheeseman, J. R.; Scalmani, G.; Barone, V.; Petersson, G. A.; Nakatsuji, H.; Li, X.; Caricato, M.; Marenich, A. V.; Bloino, J.; Janesko, B. G.; Gomperts, R.; Mennucci, B.; Hratchian, H. P.; Ortiz, J. V.; Izmaylov, A. F.; Sonnenberg, J. L.; Williams; Ding,

F.; Lipparini, F.; Egidi, F.; Goings, J.; Peng, B.; Petrone, A.; Henderson, T.; Ranasinghe, D.; Zakrzewski, V. G.; Gao, J.; Rega, N.; Zheng, G.; Liang, W.; Hada, M.; Ehara, M.; Toyota, K.; Fukuda, R.; Hasegawa, J.; Ishida, M.; Nakajima, T.; Honda, Y.; Kitao, O.; Nakai, H.; Vreven, T.; Throssell, K.; Montgomery Jr., J. A.; Peralta, J. E.; Ogliaro, F.; Bearpark, M. J.; Heyd, J. J.; Brothers, E. N.; Kudin, K. N.; Staroverov, V. N.; Keith, T. A.; Kobayashi, R.; Normand, J.; Raghavachari, K.; Rendell, A. P.; Burant, J. C.; Iyengar, S. S.; Tomasi, J.; Cossi, M.; Millam, J. M.; Klene, M.; Adamo, C.; Cammi, R.; Ochterski, J. W.; Martin, R. L.; Morokuma, K.; Farkas, O.; Foresman, J. B.; Fox, D. J. Wallingford, CT, 2016.